Journal of Petroleum Science and Technology 10 (2020) 20-29
DOI:10.22078/jpst.2020.3825.1605

Journal of Petroleum Science and Technology

https://jpst.ripi.ir/

Evaluation of Faults Reactivation Tenacity in One of the Low-Pressure SW Iranian Carbonate Reservoirs: An IOR Viewpoint

Mohsen Ezati[1], Mehran Azizzadeh[1]*, Mohammad Ali Riahi[2], Vahidoddin Fattahpour[3], and Javad Honarmand[1]

[1]*Petroleum Geology Department, Upstream Oil Industry Research and Development Center, Research Institute of Petroleum Industry (RIPI), Tehran, Iran*
[2]*Institute of Geophysics, University of Tehran, Tehran, Iran*
[3]*School of Mining Engineering, University of Tehran, Tehran, Iran*

Abstract

In case of a decrease in reservoir pressure, injection projects are inevitable that the desired production rate is maintained. Moreover, one of the key issues in injection operations is optimum injection pressure determination to prevent fault reactivation . The aim of this study is to evaluate fault reactivation tenacity in one of SW Iranian oil fields at different injection stages. Two main steps in this study are geomechanical modeling and fault extraction. In addition, fullset data, image log, dipole sonic log, and MDT pressure points were used to construct the geomechanical model. Also, 3-D seismic data were used for fault extraction and characterization. Ultimately, according to the geomechanical model, the stress state is strike-slip normal, and the maximum horizontal stress direction is toward NE-SW. Furthermore, 18 faults have been extracted using seismic data, which their strikes are often NW-SE. In addition, the faults are inactive in the present-day stress state, but the first fault will be reactivated with a 33 MPa increase in pore pressure.

Key words: Fault Reactivation, Geomechanical Modeling, Pore Pressure, Sarvak Formation

Introduction

Reactivation tendency analysis of pre-existing faults was firstly introduced by Morris et al in 1996 [1]. In this analysis, it is assumed that in a given stress field, the tendency of a fault surface to slip depends on the coefficient of internal friction and the ratio of shear to normal stress. The earth's crust contains broadly distributed faults in many different sizes and orientations, and magnitudes of the principal stresses at depth are constrained by the frictional strength of these faults [2]. The pore pressure changes during injection or production cause a change into the stress state, which is known as pore pressure–stress coupling (PSC) . Therefore, it is important to understand PSC throughout an oil or gas field development to assess the fault reactivation risks and cap-rock integrity potential damage during reservoir depletion and injection processes [3].

Over the past decade, the possible consequences related to the fault reactivation have been studied by researchers. Loss of the cap-rock integrity by developing leakage conduits [4-6] and induced seismicity [7,8,9], are two cases of this issue. Analytical and numerical methods are used to evaluate reactivation tenacity of faults. Numerical simulation of reservoir pore pressure enhancement has been investigated in the literature [10, 11, 12, 13, 14, 15]. One of the important steps for an injection project is site characterization and selection [16,17]. Site selection has been studied in the literature [18-21]. The primary stage for the site characterization is the geomechanical assessment of the reservoir and cap-rock system. It is implemented to detect geological [22] and mechanical characteristics of the site to ensure effective operation.

The first step in evaluating the reactivation potential of faults is to construct 1-D geomechanical models [23-26]. In a complete 1-D geomechanical model, the rock mechanical properties, pore pressure, and principal in situ stress (their orientation and magnitude) will be defined for a distinct stratigraphic or lithology interval [27-30]. In addition to evaluating the faults reactivation tenacity, 1-D geomechanical model can be used to mitigate the geomechanical issues in association with (1) Improved Oil Recovery (IOR), (2) hydraulic fracturing, overpressures, (3) wellbore stability, and (4) sand production [31-33].

Before the injection, accurate faults extraction is important for PSC analysis. The orientation and dip of the faults are important parameters that should

**Corresponding author:* Mehran Azizzadeh, Petroleum Geology Department, Upstream Oil Industry Research and Development Center, Research Institute of Petroleum Industry (RIPI), Tehran, Iran
E-mail addresses: azizzadehm@ripi.ir
Received 2019-07-15, Received in revised form 2019-12-01, Accepted 2020-01-22, 2020-06-14

be identified. In this study, 3-D seismic data were used to identify the faults.

Sarvak Formation is the second oil reservoir of Iran (after the Asmari Formation). This formation contains more than 20% of the oil-in-place of Iran [34].

In the studied field, oil has been continuously produced from the Sarvak reservoir over the past 20 years, so its pore pressure is decreased and is close to the hydrostatic state. To prevent a major decline in production, injection projects must be considered in the future.

The aim of this study was to estimate the present-day stress magnitudes and orientations in the studied oilfield and investigate the fault stability in both current and after injection conditions. In this paper, a comprehensive data set was used to construct a 1D Mechanical Earth Model (MEM) of the Sarvak reservoir for the pore pressure enhancement at one of the oil fields of Abadan plain. It was carried out using geological properties, Fullset log data, dynamic and static rock mechanical properties, pore pressure data, drilling reports, and faults' studies. The present time pore pressure of the Sarvak reservoir was estimated based on the modified Eaton method. The magnitudes of in-situ horizontal stresses are estimated based on the poroelastic method and calibrated using Formation integrity test (FIT), stress polygon, mud-loss data, wellbore failures observations, and modular formation dynamics tester (MDT) data. The orientations of horizontal in-situ stress were determined according to borehole breakouts. The effect of increasing pressure on stresses was analyzed using PSC theory. Ultimately, the maximum tolerable injection pressure was estimated. According to this study, the obtained results can be used as a basis for the future field management and development plans.

Geological Setting

The studied oil field is an N-S trending anticline, which is situated in Abadan Plain, southwest Iran. Moreover, this oil field is located 80 km west of Ahvaz city (Figure 1). Also, Abadan Plain has three major structural trends: N–S, NW–SE, and NE–SW, which are associated with the deep-seated faults activations [35]. In addition, the structures with these trends are related to reactivation of the basement-rooted normal faults which caused forced-folding in overlaying sediments [35].

Fig. 1 The location of the studied oil field in Abadan Plain, SW Iran

Abadan Plain is part of the Mesopotamia sedimentary basin, which is the northern margin of the Arabian platform. The Sarvak Formation was deposited during the late Albian to early Turonian in upper Cretaceous [36]. In Abadan Plain, the Sarvak Formation is overlain by Laffan Formation, and its lower contact is with Kazhdumi Formation (Figure 2). The Sarvak Formation in south Iran is equivalent to the Mauddud, Ahmadi, Rumaila and Mishrif Formations in southeast Iraq [37]. In the studied field, the Sarvak Formation comprises thick limestone with minor clayey and argillaceous intervals, reaching totally 600 to 700 m in thickness [38]. Moreover, there are a few fracture intervals in the Sarvak reservoir of the studied oil field [39].

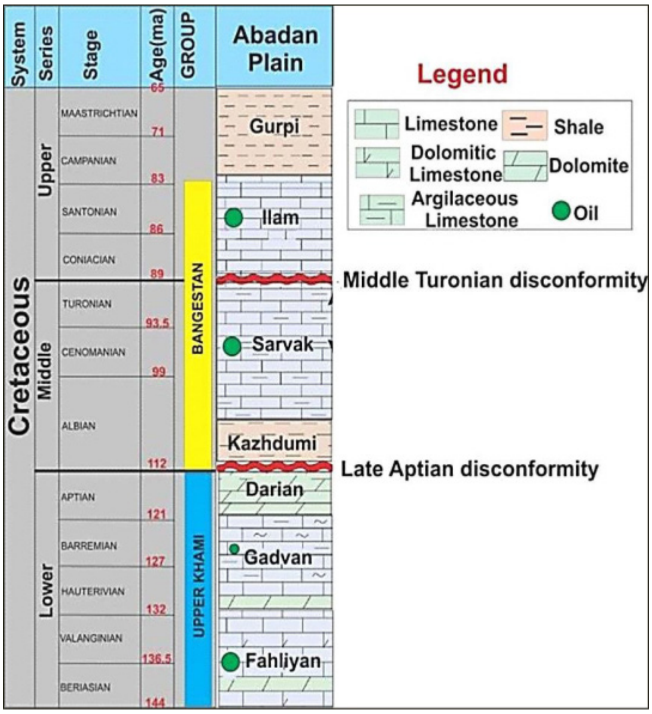

Fig. 2 The Cretaceous stratigraphic column of Abadan Plain (modified from [40])

Materials and Methods

Available data

Materials

In this study, fullset logs such as CAL (Caliper), BS (Bit Size), GR (Gamma-ray), RHOB (Bulk Density), NPHI (Neutron Porosity), DTP (Slowness of compressional wave), PEF (Photoelectric Factor), and resistivity logs were used for the petrophysical evaluation, overburden stress measurement, and elastic modulus calculation. FMI (Fullbore Formation Microimager) was utilized to detect the wellbore failures and, subsequently, horizontal stresses' directions. DSI (Dipole Shear Sonic Imager) data were used to extract DTS (Slowness of shear wave) for the elastic modulus calculation. Moreover, MDT (Modular Formation Dynamics Tester) pressure points were used to calibrate the pore pressure curves. Also, wellbore failures, drilling reports, and FIT (Formation Integrity Test) data were used for the 1-D geomechanical model validation. Moreover, 3-D seismic data were used for the faults extraction.

Methods

Geomechanical Modeling

A geomechanical model is a numerical presentation of the geomechanical properties of a formation. In addition to petrophysical characteristics (e.g., lithology, density, and porosity), a 1-D geomechanical model includes pore pressures, stress state, and rock mechanical properties. The flowchart, which is used for 1-D geomechanical modeling, is shown in Figure 3.

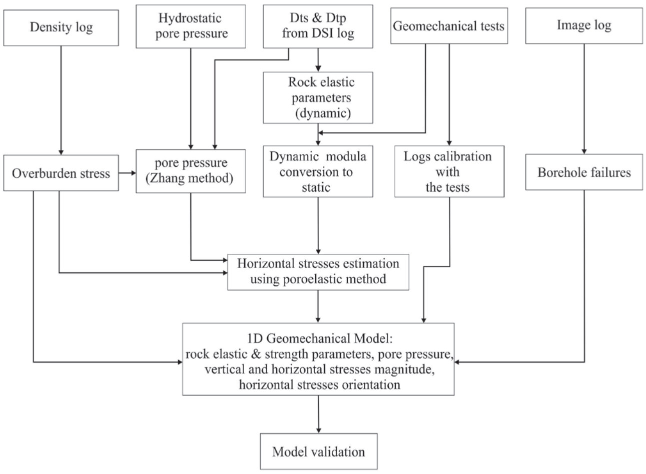

Fig.3 The flowchart used for the 1-D geomechanical modeling

Rock Elastic Properties

The dynamic Poisson's ratio (ν_d) and dynamic Young's modulus (E_d) were calculated using compressional wave velocity (V_P), shear wave velocity (V_S), and density of rock (ρ), as they are calculated using the following equations (Equations 1 and 2) [41]:

$$E_d=\rho V_S^2\frac{3V_P^2-4V_S^2}{V_P^2-V_S^2} \tag{1}$$

$$\nu_d=\frac{V_P^2-2V_S^2}{2\left(V_P^2-V_S^2\right)} \tag{2}$$

Pore Pressure

Pore pressure can be measured directly (in separate points) using MDT, RFT (Repeat Formation Tester), and DST (Drill Stem Test) data. Also, pore pressure is estimated by empirical relationships and petrophysical logs [42]. The Eaton equation [43] is one of the methods which is used to estimate formation pore pressure and defined as:

$$P_{Pg}=S_V-(S_V-P_{Hyd})\left(\frac{NCT}{DT}\right)^3 \tag{3}$$

where P_{Pg} is pore pressure gradient, S_V is vertical stress, P_{Hyd} is hydrostatic pore pressure gradient, NCT is a normal compaction trend, and D_T is the slowness of compressional wave. Also, the Eaton equation has been modified by Zhang in 2011, as seen in the following equation (i.e. Equation 4) [42]:

$$P_{Pg}=S_V-(S_V-P_{Hyd})\left(\frac{DT_m+\left(DT_{ml}-DT_m\right)e^{-cZ}}{DT}\right)^3 \tag{4}$$

where DT_m is compressional wave slowness in shale lithology (with zero porosity), DT_{ml} is compressional wave slowness in drilling mud, c is an experimental constant, and Z is the depth.

In this study, a good correlation between MDT points and the estimated pore pressure curve is achieved by considering c=0.0005 and the coefficient power equal to 0.44 respectively. In future studies, these coefficients can be used to estimate the pore pressure of Sarvak Formation.

Principal Stresses

In general, the dominant stresses in one region are expressed in three principal stresses that consist of one vertical stress and two horizontal stresses. The vertical stress (S_v) was calculated using the overburden weight, as seen in Equation 5 [44]:

$$S_V=\int_0^z \rho(z)g\,dz \tag{5}$$

where z is the depth, ρ(z) is rock density (as a function of depth), and g is Earth's gravity acceleration. The poroelastic equations (i.e. Equations 6 and 7) were used to estimate the minimum (S_{hmin}) and maximum (S_{Hmax}) horizontal stresses [41]:

$$S_{hmin}=\frac{\nu}{(1-\nu)}\left(S_V-\alpha PP\right)+\alpha PP+\frac{E_S}{\left(1-\nu^2\right)}\varepsilon_x+\frac{\nu\times E_S}{\left(1-\nu^2\right)}\varepsilon_y \tag{6}$$

$$S_{Hmax}=\frac{\nu}{(1-\nu)}\left(S_V-\alpha PP\right)+\alpha PP+\frac{E_S}{\left(1-\nu^2\right)}\varepsilon_y+\frac{\nu\times E_S}{\left(1-\nu^2\right)}\varepsilon_x \tag{7}$$

where ν is Poisson's ratio, S_V is vertical (overburden) stress, α is Biot's coefficient (which considered equal to 1), PP is pore pressure, and E_S is static Young's modulus. Furthermore, the tectonic strain on x (ε_x) and y (ε_y) axes were calculated using the following equations (i.e. Equations 8 and 9) [9]:

$$\varepsilon_x=\frac{S_V\times\nu}{E_S}\left(\frac{1}{1-\nu}-1\right) \tag{8}$$

$$\varepsilon_y=\frac{S_V\times\nu}{E_S}\left(1-\frac{\nu^2}{1-\nu}\right) \tag{9}$$

Also, the FMI image log was used to determine the principal horizontal stresses' directions from the wellbore breakouts.

Principal Stresses' Changes Due to Injection

To assess the faults reactivation potential, shear and normal stresses on fault planes are necessary to be calculated [2]. 3-D Mohr's diagram is used for this analysis (Figure 4). The values of the three principal stresses are needed to represent 3-D Mohr's circles. Each of the faults can be shown by a point, situated in the space between the two smaller Mohr's circles, and the big Mohr's circle (Figure 4). The position of fault plane in the 3-D Mohr's circle is determined using β_1 and β_3 angles. These angles are between the normal to the fault and the S_1 and S_3 axes respectively. Moreover, to find the location of the fault plain point, the angles $2\beta_1$ and $2\beta_3$ are used to find points on the two small circles, and by creating arcs drawn from the center of the other Mohr's circle, the fault plane point is determined as the intersection of the two arcs (Figure 4).

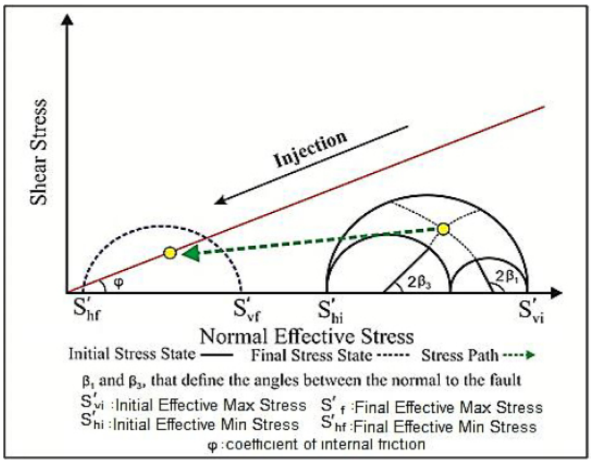

Fig. 4 The displacement mechanism of the Mohr's circle due to the injection and reactivation of pre-existing faults (modified from [1])

Induced vertical stress change caused by pore pressure changes can be negligible for laterally infinitely extended thin reservoirs [45]. But in the horizontal direction, due to confinement by surrounding rock bodies, change of horizontal stresses might be significant [9,46]. By using the assumption of uniaxial strain (oedometric) conditions, under constant vertical stress, the change of in situ horizontal stress can be calculated by Equation 10 [21]:

$$\Delta S_{Hor} = \alpha \frac{(1-2\nu)}{(1-\nu)} \Delta P_P \quad (10)$$

where ΔS_{Hor} is horizontal stress change, α is Biot's coefficient, ν is Poisson's ratio, and ΔP_P is the pore pressure changes (due to injection or depletion).

Results and Discussion

1-D geomechanical model

In Figure 5, the 1-D geomechanical model of well-A is shown. In this model, the elastic/strength parameters of rock, stresses, and pore pressure are presented. In well-A, the magnitude of S_{Hmax} is mostly equal to S_V, and these two stresses are larger than S_{hmin}, indicating that the stress state is strike-slip normal (S_{Hmax}=S_V>S_{hmin}). In Table 1, the averages of stress/pore pressure parameters of the present-day are shown. Accordingly, the average of S_{Hmax} is slightly higher than that of S_V. Also, based on the 1-D geomechanical model, the Poisson's ratio average is equal to 0.31.

Table 1 The averages of stress/pore pressure parameters in well-A

S_{Hmax} (MPa)	S_V (MPa)	S_{hmin} (MPa)	P_P (MPa)
70.47	69.32	61.78	34.30

Moreover, it seems that the constants suggested by this research (c=0.0005 and the coefficient power=0.44) to estimate pore pressure are suitable for the Sarvak Formation in the studied field. The pore pressure of the Sarvak reservoir is low and close to the hydrostatic pressure (P_{Hyd}). Therefore, if the production continues from the reservoir, its pore pressure falls below the hydrostatic level, and subsequently, the reservoir will not be able to produce, naturally. In addition, a further decrease in pore pressure may cause mud loss during drilling in the Sarvak reservoir. Therefore, pore pressure enhancement projects should be included in field development plans to avoid these problems.

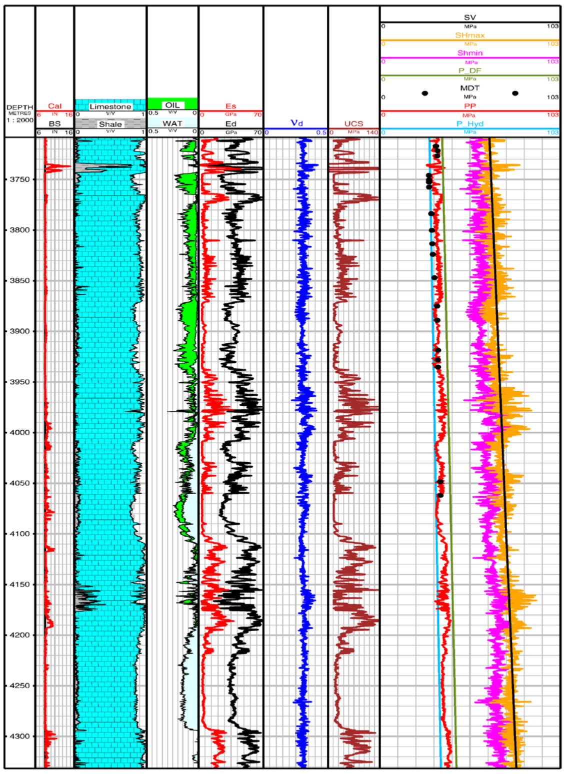

Fig. 5 1-D geomechanical model of well-A. The stress state in this well is a strike-slip normal, and the pore pressure is close to the hydrostatic pressure. The tracks from left to right are depth, caliper-bit size, lithology, oil/water saturation, Young's modulus, Poisson's ratio, UCS, and stresses/pressures.

The Borehole breakouts that picked from FMI were used to determine the direction of horizontal stresses. In Figure 6, a pair of breakouts, which has been picked on the FMI image log, is shown.
When the calipers of FMI faced with a pair of breakouts, one of its clippers (C1) became larger than the other one (C2) and bit size, as seen in Figure 6. This method was used for cross-checking of the image-derived breakouts.

A total of 94 borehole breakouts were identified in the well-A. According to the breakouts orientation, the S_{hmin} and S_{Hmax} directions are N40°W and N60°E respectively (Figure 7). The total length of the breakouts and the standard deviation of their orientation are 109 m and 6.5°, respectively. Hence, based on the quality ranking system of the stress direction indicators [1], the quality of determined horizontal stress directions is “A”.

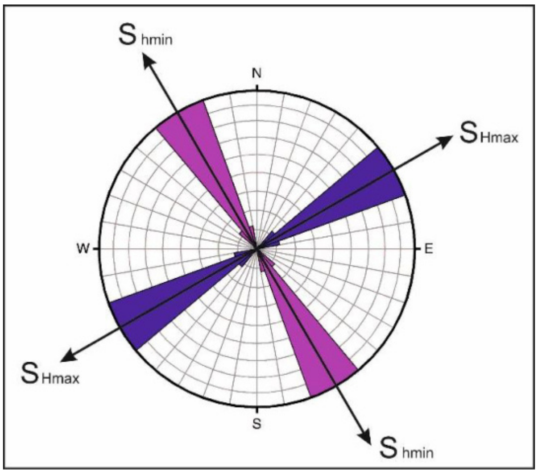

Fig. 7 S_{Hmax} and S_{hmin} directions from borehole breakouts interpretation.

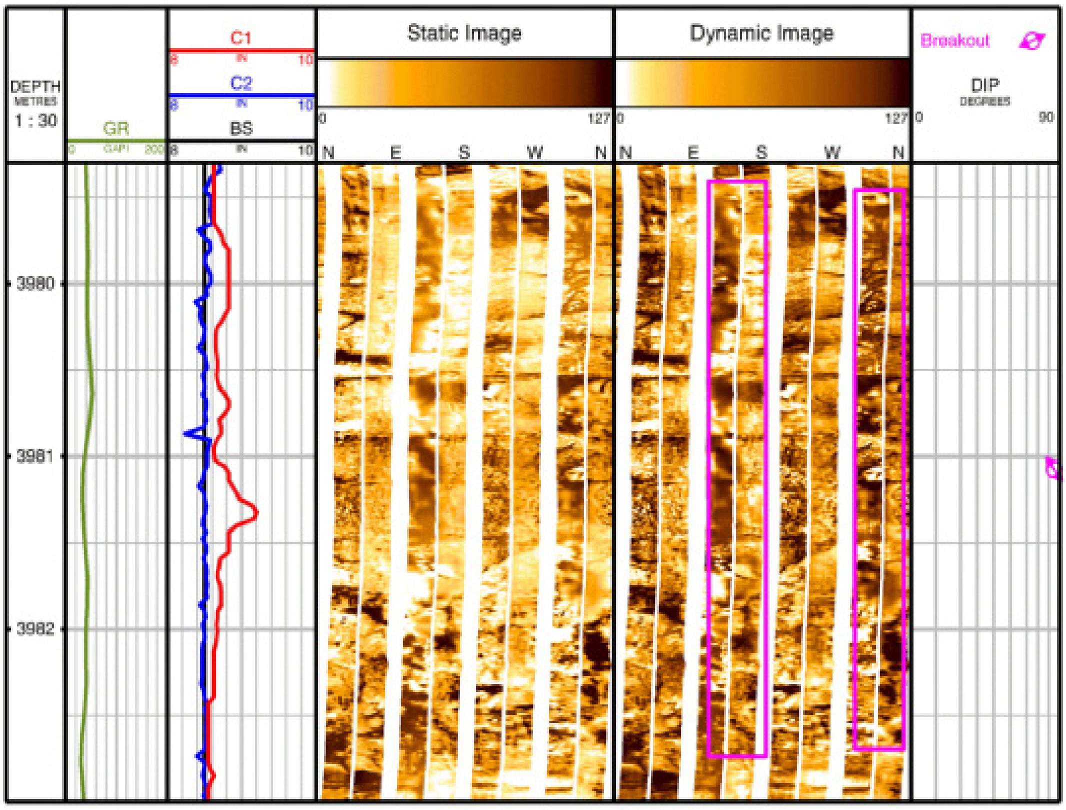

Fig. 6 A pair of breakouts in well-A that is marked with purple boxes on the FMI dynamic image. The tracks from left to right are depth, gamma-ray, the two calipers of FMI and bit size, static image, dynamic image, and event signs

The 1-D geomechanical model was validated using FIT data, stress polygon, mud-loss data, breakouts, and MDT data. The values of the FIT points were less than the minimum horizontal stress (Figures 8-A and B).
Borehole breakouts were observed at a depth 3765.2 meters, so the allowable states are above the green line in the stress polygon (Figure 8-C). Hence, strike-slip and reverse states are allowable at a depth of 3765.2 meters. Accordingly, the strike-slip stress state was determined at this depth using poroelastic equations. On the other hand, at a depth of 3908.24 meters, borehole breakouts are not observed (Figure 8-D); hence, the permitted stress state is below the green line, where only normal stress state is allowable (Figure 8-D). Correspondingly, the normal stress state was obtained at this depth using poroelastic equations (Figure 8-D).
During drilling into Ilam Formation , at first, mud weight (PW_Loss) was 87 pcf, which was accompanied by a complete mud-loss. As shown in Figure 8-E, the 87 pcf drilling mud pressure touched S_{hmin}, which was predicted by the 1D model. Once the total loss occurred in the Ilam Formation, the mud weight was reduced to 85 pcf (PW), and drilling was continued.
Breakout pressure was calculated using the calculated stresses and Mohr-Coulomb and Mogi-Coulomb failure criteria (Figure 8-F). Moreover, according to Figure 8-F, the drilling mud pressure falls in the breakout area of both criteria, and the FMI image log also shows the widespread presence of borehole breakouts in the well.

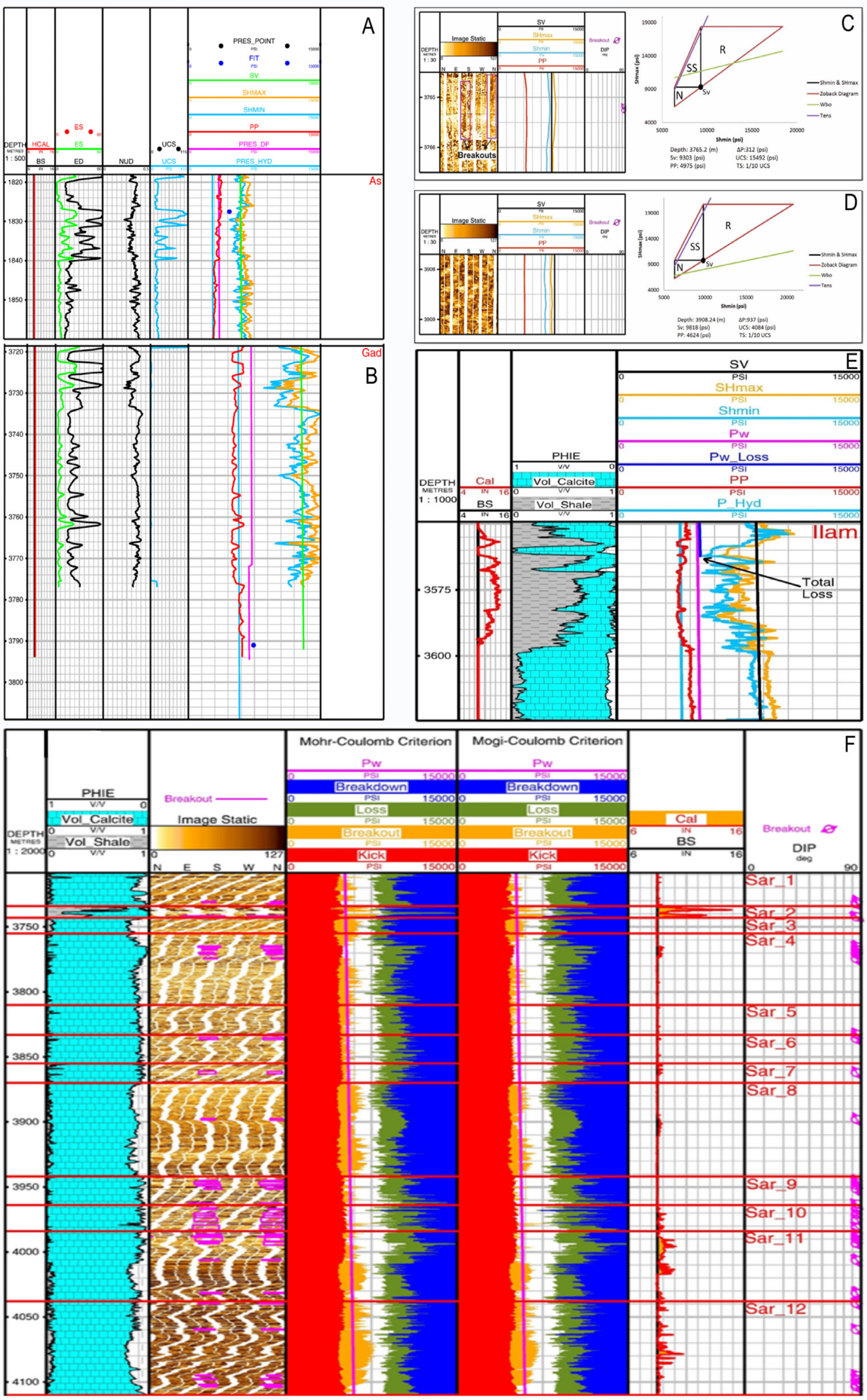

Fig. 8 1-D geomechanical model validation methods: A and B) FIT data, C and D) stress polygon, E) mud-loss data and F) wellbore failures' observations

Faults Properties

Ant-tracking attribute and manual editing methods have been run to interpret the faults. After that, wavelet extraction and well to seismic tie were carried out to calculate the fault characteristics,18 faults were interpreted in the Cretaceous horizon of the studied oil field using 3-D seismic data (Figure 9). These faults are located in the northwest of the field, and their major displacement mechanism is strike-slip with a minor dip-slip (normal) component. Moreover, the average strike-slip and dip-slip displacements are 1 km and 100 m respectively. Also, some of these faults continue upward to the Tarbur Formation, and some of them reach downward to the Garu Formation.

Each fault was identified by a number (Table 2). In this table, dip and strike of the faults are presented. According to this table, the strike of all faults, except the fault-12, is NW-SE; in addition, the strike of fault-12 is NE-SW (Table 2).

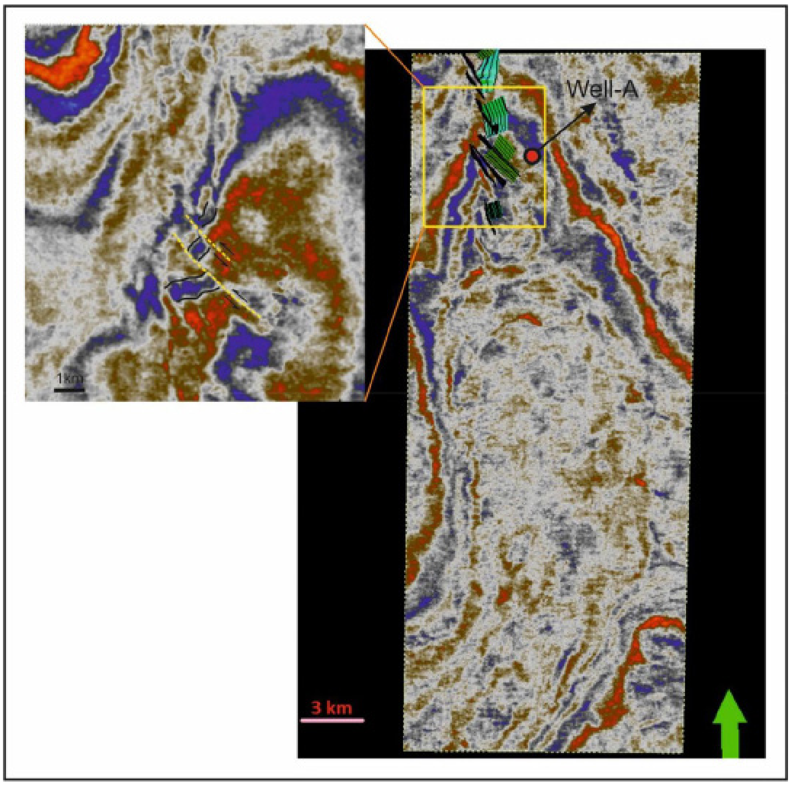

Fig. 9 The Cretaceous horizon faults on seismic time slices and the position of well-A relative to them. The strike-slip movement of two faults is shown on the left time slice

Table 2 Dip and dip direction of the identified faults.

Fault ID	Dip (deg)	Dip Direction Azimuth (deg)
1	55.03	55
2	73.79	235
3	45.84	229
4	46.32	63
5	44.85	227
6	39.24	237
7	52.21	74
8	59.38	48
9	68.58	232
10	53.47	225
11	52.02	54
12	56.13	278
13	56.83	230
14	43.29	32
15	37.38	66
16	35.10	265
17	48.16	267
18	52.58	53

The Cretaceous faults' poles were plotted using Scheidt net (Figure 10-A). This stereonet indicates that the dip of the faults is mainly toward NE and SW. Hence, generally, the dip directions of these faults are perpendicular to each other. According to the rose diagram of the faults, their strikes are mainly uniform and are toward NW-SE. But the strike of fault-12 is NE-SW, and the strikes of fault-16 and fault-17 are close to that.

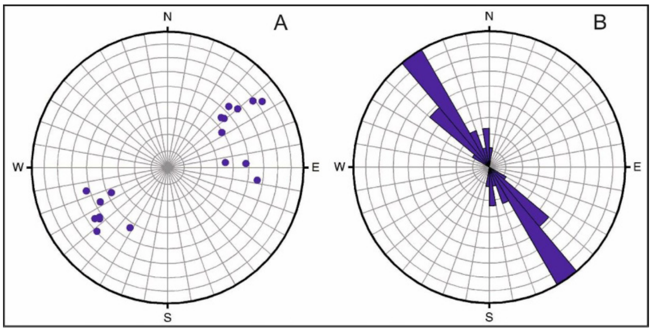

Fig. 10 The dip directions of the faults are mainly toward NE and SW. A: Stereonet of the faults (lower hemisphere of Scheidt net), B: Rose-diagram of the faults

Faults Reactivation Analysis

PSC analysis was used to calculate the maximum sustainable injection pressure. Moreover, this analysis was performed using MohrPlotter software.
For the PSC analysis, firstly, normal and shear stresses on the fault planes were calculated. S_{Hmax} directional is approximately perpendicular to the faults strike (Figure 11). S_{Hmax} directional is NE-SW, and the strike of all faults, except fault-12 (Table 2), is NW-SE.

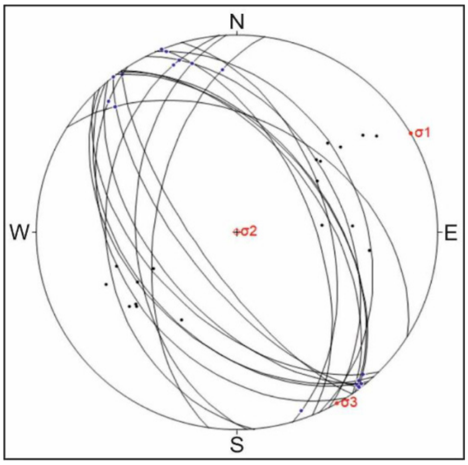

Fig.11 The dip and strike of faults and the orientations of principal stresses

To evaluate the fault activity in the present time, fault planes were plotted on 3-D Mohr's circle (Figure 12). Moreover, each of the fault points on 3D Mohr's circle has a long distance from Mohr's envelope. Hence, in the present-day stress state, these faults are inactive.
Regarding the present-day stress state and the faults' orientations, maximum tolerable injection pressure, before the first fault reactivation, is equal to 33 MPa (Figure 12-B). Fault-12 has the most suitable orientation for reactivation than the other faults. Furthermore, fault-16 and fault-17, which their orientations are more close to fault-12, will be reactivated, secondly.
According to PSC theory, during injection, in addition to Mohr's circle displacement, its size changes. Also, during the injection, the stress state can be changed. The current stress state is strike-slip normal, but with a 20 MPa increase in pore pressure, the stress state changes into reverse (Table 3). Also, with the 33 MPa increase in pore pressure, the first fault touches the mohr's envelope (Figure 12).

Table 3 Changes in principal effective stresses during pore pressure increase at different stages.

Pore Pressure Increase (MPa)	S'_{Hmax} (MPa)	S'_{V} (MPa)	S'_{hmin} (MPa)
10	31.67	25.02	22.98
20	27.18	15.02	18.48
33	21.34	2.02	12.65

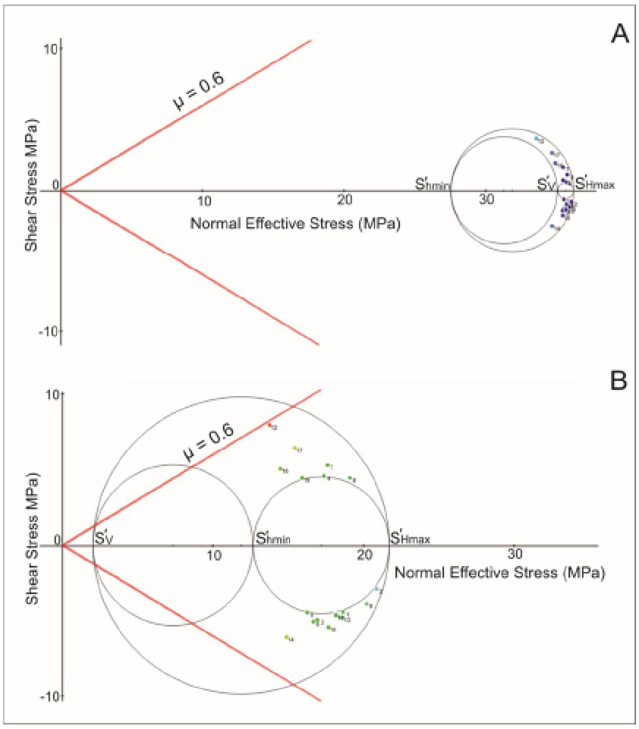

Fig. 12 3D Mohr's circles and the position of the faults on the circles. The faults are inactive at the current stress state, but they will be reactivated with a 33 MPa increase in pore pressure. A: The initial (present-day) stress state, B: The stress state after injection and an increase in pore pressure by 33 MPa

Conclusions

In this study, the fault reactivation tenacity due to the injection was assessed in one of the SW Iranian oil fields. For this purpose, a 1-D geomechanical model was constructed, and then the faults were extracted. Afterward, the tendency to the activity of faults in the present stress state and during injection was evaluated. Finally, the following results were obtained:

• The present-day stress state is strike-slip normal stress state, and S_{Hmax} direction is toward NE-SW.
• The pore pressure of the Sarvak reservoir of the studied field is low and close to hydrostatic pore pressure.
• 18 faults were identified in the Cretaceous horizon of the studied oil field. These faults are located in the northwest of the field, and their main mechanism is a strike-slip. Moreover, the strike directions of these faults are often toward NW-SE.
• All of the faults are currently inactive in the present-day stress state.
• The first fault (i.e. fault-12) will be reactivated with a 33 MPa increase in pore pressure.

Nomenclatures

BS: Bit Size
CAL: Caliper
DSI: Dipole shear sonic imager
DST: Drill stem test
DT_P: Slowness of compressional wave
DT_S: Slowness of shear wave

E_d: Dynamic Young's modulus
E_S: Static Young's modulus
FIT: Formation integrity test
FMI: Fullbore formation microimager
g: Earth's gravity acceleration
GR: Gamma-ray
IOR: Improved oil recovery
MDT: Modular formation dynamics tester
NCT: Normal compaction trend
NPHI: Neutron porosity
DFP: Drilling fluid pressure
PEF: Photoelectric factor
pp: Pore pressure
PSC: Pore pressure–stress coupling
RFT: Repeat formation tester
RHOB: Bulk density
S_1: Maximum principal stress
S_3: Minimum principal stress
S_{Hmax}: Maximum horizontal stress
S'_{Hmax}: Effective maximum horizontal stress
S_{hmin}: Minimum horizontal stress
S'_{hmin}: Effective minimum horizontal stress
S_V: Vertical stress
S'_V: Effective vertical stress
V_P: Compressional wave velocity
V_S: Shear wave velocity
α: Biot's coefficient
ΔP_P= Pore pressure changes
ΔS_{Hor}= Horizontal stress change
μ: Coefficient of internal friction
ν: Poisson's ratio
ρ: Rock density

References

1. Morris A, Ferrill D A, Brent Henderson D B (1996) Slip-tendency analysis and fault reactivation. Geology 24: 275-278.
2. Zoback M D, (2010) Reservoir geomechanics (1st ed.). Cambridge University Press 1-445.
3. Salemi H, Rezagholilou A, Asadi S, Iglauer S, Sarmadivaleh M (2017) Poroelastic effects of pore pressure-stress coupling on fault reactivation risks during gas injection. presented at the 51st US Rock Mechanics/Geomechanics Symposium, American Rock Mechanics Association.
4. Wiprut D, Zoback M D (2002) Fault reactivation, leakage potential, and hydrocarbon column heights in the northern North Sea. Norwegian Petroleum Society Special Publications 11: 203-219.
5. Hawkes C D, McLellan P J, Bachu S (2005) Geomechanical factors affecting geological storage of CO_2 in depleted oil and gas reservoirs. Journal of Canadian Petroleum Technology 44: 52-61.
6. Langhi L, Zhang Y, Gartrell A, Underschultz J, Dewhurst D (2010) Evaluating hydrocarbon trap integrity during fault reactivation using geomechanical three-dimensional modeling: An example from Timor Sea, Australia. American Association of Petroleum Geologists Bulletin 94: 567-591.
7. Zoback M D, Gorelick S M (2012) Earthquake triggering and large scale geologic storage of carbon dioxide. Proceedings of the National Academy of Sciences 109:10164-10168.
8. Rutqvist J, Rinaldi A P, Cappa F, Moridis G J (2013) Modeling of fault reactivation and induced seismicity during hydraulic fracturing of shale-gas reservoirs. Journal of Petroleum Science and Engineering 107: 31-44.
9. Rutqvist J, Birkholzer J, Cappa F, Tsang C F (2007) Estimating maximum sustainable injection pressure during geological sequestration of CO_2 using coupled fluid flow and geomechanical fault-slip analysis. Energy Conversion and Management 48(6): 1798-1807.
10. Safi R, Agarwal R K, Banerjee S (2016) Numerical simulation and optimization of CO_2 utilization for enhanced oil recovery from depleted reservoirs. Chemical Engineering Science 144: 30–38.
11. Tambach T J, Koenen M, Wasch L J, Van Bergen F (2015) Geochemical evaluation of CO_2 injection and containment in a depletedgas field. International Journal of Greenhouse Gas Control 32: 61–80.
12. Perera M, Gamage R, Rathnaweera T, Ranathunga A, Koay A, Choi X (2016) A review of CO_2-enhanced oil recovery with a simulated sensitivity analysis. Energies 9: 481.
13. Vilarrasa V, Makhnenko R, and Gheibi S (2016) Geomechanical analysis of the influence of CO_2 injection location on fault stability. Journal of Rock Mechanics and Geotechnical Engineering 8: 805–818.
14. Ren B, Duncan I J (2019) Reservoir simulation of carbon storage associated with CO_2 EOR in residual oil zones, San Andres formation of West Texas, Permian Basin, USA. Energy 167: 391–401.
15. Haro HAV, Paula Gomes M S, Rodrigues L G (2018) Numerical analysis of carbon dioxide injection into a high permeability layer for CO_2-EOR projects. Journal of Petroleum Science and Engineering 171: 164–174.
16. Keating E, Bacon D, Carroll S, Mansoor K, Sun Y, Zheng L, Harp D, Dai Z (2016) Applicability of aquifer impact models to support decisions at CO_2 sequestration sites. International Journal of Greenhouse Gas Control 52: 319–330.
17. Ganguli S S, Vedanti N, Dimri V P (2016) 4D reservoir characterization using well log data for feasible CO_2-enhanced oil recovery at Ankleshwar, Cambay Basin-A rock physics diagnostic and modeling approach. Journal of Applied Geophysics 135: 111–121.
18. Rodosta T D, Litynski J T, Plasynski S I, Hickman S, Frailey S, Myer L (2011) Site selection and initial characterization for storage of CO_2 in deep geological formations. Energy Procedia 4: 4664-4671.
19. Vilarrasa V, Carrera J, Olivella S (2013) Hydromechanical characterization of CO_2 injection sites. International Journal of Greenhouse Gas Control 19: 665–677.
20. Colucci F, Guandalini R, Macini P, Mesini E, Moia F, Savoca D (2016) A feasibility study for CO_2 geological storage in Northern Italy. International Journal of Greenhouse Gas Control 55: 1–14.
21. Dai Z, Zhang Y, Bielicki J, Amooie M. A, Zhang M, Yang C, Zou Y, Ampomah W, Xiao T, Jia W, Middleton R (2018) Heterogeneity-assisted carbon dioxide storage

in marine sediments. Applied Energy 225: 876–883.

22. Colucci F, Guandalini R, Macini P, Mesini E, Moia F, Savoca D (2016) A feasibility study for CO_2 geological storage in Northern Italy. International Journal of Greenhouse Gas Control 55: 1–14.
23. Dai Z, Viswanathan H, Fessenden-Rahn J, Middleton R, Pan F, Jia W, Lee S Y, McPherson B, Ampomah W, Grigg R (2014) Uncertainty quantification for CO_2 sequestration and enhanced oil recovery. Energy Procedia 63: 7685-7693.
24. Keating E, Bacon D, Carroll S, Mansoor K, Sun Y, Zheng L, Harp D, Dai Z (2016) Applicability of aquifer impact models to support decisions at CO_2 sequestration sites. International Journal of Greenhouse Gas Control 52: 319-330.
25. Ampomah W, Balch R S, Cather M, Will R, Gunda D, Dai Z, Soltanian M R (2017) Optimum design of CO_2 storage and oil recovery under geological uncertainty. Applied Energy 195: 80-92.
26. Amiri M, Lashkaripour G R, Ghabezloo S, Moghaddas N H, Tajareh M H (2019) Mechanical earth modeling and fault reactivation analysis for CO_2-enhanced oil recovery in Gachsaran oil field, south-west of Iran. Environmental Earth Sciences 78: 112.
27. Darvish H, Nouri-Taleghani M, Shokrollahi A, Tatar A, (2015) Geo-mechanical modeling and selection of suitable layer for hydraulic fracturing operation in an oil reservoir (south west of Iran). Journal of African Earth Sciences 111: 409-420.
28. Bozorgi E, Javani D, Rastegarnia M (2016) Development of a mechanical earth model in an Iranian off-shore gas field. Journal of Mining and Environment 7(1): 37-46.
29. Kidambi T, Kumar G S (2016) Mechanical Earth Modeling for a vertical well drilled in a naturally fractured tight carbonate gas reservoir in the Persian Gulf. Journal of Petroleum Science and Engineering 141: 38-51.
30. Aghajanpour A, Fallahzadeh S H, Khatibi S, Hossain M M, Kadkhodaie A (2017) Full waveform acoustic data as an aid in reducing uncertainty of mud window design in the absence of leak-off test. Journal of Natural Gas Science and Engineering 45: 786-796.
31. Plumb R, Edwards S, Pidcock G, Lee D, Stacey B, (2000) The mechanical earth model concept and its application to high-risk well construction projects. In IADC/SPE Drilling Conference, Society of Petroleum Engineers.
32. Rutqvist J, Cappa F, Rinaldi A P, Godano M (2014) Modeling of induced seismicity and ground vibrations associated with geologic CO_2 storage, and assessing their effects on surface structures and human perception.International Journal of Greenhouse Gas Control 24: 64-77.
33. Niu Z, Li Q, Wei X, Li X, Ma J (2017) Numerical investigation of slippage characteristics of normal and reverse faults under fluid injection and production. Environmental Earth Sciences 76(14): 502.
34. Motiei H, (1993) Stratigraphy of Zagros, Treatise on the Geology of Iran (1st ed.). Geological Survey and Mineral Exploration of Iran (GSI). 151: In Persian.
35. Abdollahie-Fard I, Braathen A, Mokhtari M, Alavi S A (2006) Interaction of the Zagros Fold-Thrust Belt and the Arabian-type, deepseated folds in the Abadan Plain and the Dezful Embayment, SW Iran. Petroleum Geoscience 12: 347–362.
36. Motiei H (2010) An Introduction to Zagros Petroleum Reservoirs Evaluation, (for geologist) (1st ed.). Geological Survey and Mineral Exploration of Iran (GSI) 2: 681, In Persian.
37. Nairn A E M, Alsharhan A S (1997) Sedimentary basins and petroleum geology of the Middle East. Elsevier.
38. Assadi A, Honarmand J, Moallemi S A, Abdollahie-Fard I (2016) Depositional environments and sequence stratigraphy of the Sarvak Formation in an oil field in the Abadan Plain, SW Iran. Facies 62(4): 1-22.
39. Ezati M, Azizzadeh M, Riahi M A, Fattahpour V, Honarmand J (2018) Characterization of micro-fractures in carbonate Sarvak reservoir, using petrophysical and geological data, SW Iran. Journal of Petroleum Science and Engineering 170: 675-695.
40. Christian L (1997) Cretaceous Subsurface Geology of the Middle East Region. GeoArabia 2: 239-256.
41. Fjaer E, Holt R M, Raaen A M, Risnes R, Horsrud P (2008) Petroleum related rock mechanics (2nd ed.), Developments in Petroleum Science. Elsevier 53: 1-483.
42. Zhang J (2011)Pore pressure prediction from well logs: Methods, modifications, and new approaches. Earth-Science Reviews 108(1): 50-63.
43. Eaton B. A (1975) The equation for geopressure prediction from well logs. Fall Meeting of the Society of Petroleum Engineers of AIME, Dallas, Texas.
44. Jaeger J C, Cook N G (1969) Fundamentals of Rock Mechanics. Methuen, London, New York: Barnes and Noble 593.
45. Hillis R (2000) Pore pressure/stress coupling and its implications for seismicity. Exploration Geophysics 31(2): 448-454.
46. Streit J E, Hillis R R (2004) Estimating fault stability and sustainable fluid pressures for underground storage of CO_2 in porous rock. Energy 29(9-10): 1445-1456.